

Turbulent boundary layers over substrates with streamwise-preferential permeability

Hartog, Friso H.; Van Nesselrooij, Michiel; Van Campenhout, Olaf W.G.; Schrijer, Ferry F.J.; Van Oudheusden, Bas W.; Masania, Kunal

DOI

[10.1103/PhysRevFluids.9.114602](https://doi.org/10.1103/PhysRevFluids.9.114602)

Publication date

2024

Document Version

Final published version

Published in

Physical Review Fluids

Citation (APA)

Hartog, F. H., Van Nesselrooij, M., Van Campenhout, O. W. G., Schrijer, F. F. J., Van Oudheusden, B. W., & Masania, K. (2024). Turbulent boundary layers over substrates with streamwise-preferential permeability. *Physical Review Fluids*, 9(11), Article 114602. <https://doi.org/10.1103/PhysRevFluids.9.114602>

Important note

To cite this publication, please use the final published version (if applicable).
Please check the document version above.

Copyright

Other than for strictly personal use, it is not permitted to download, forward or distribute the text or part of it, without the consent of the author(s) and/or copyright holder(s), unless the work is under an open content license such as Creative Commons.

Takedown policy

Please contact us and provide details if you believe this document breaches copyrights.
We will remove access to the work immediately and investigate your claim.

Green Open Access added to TU Delft Institutional Repository

'You share, we take care!' - Taverne project

<https://www.openaccess.nl/en/you-share-we-take-care>

Otherwise as indicated in the copyright section: the publisher is the copyright holder of this work and the author uses the Dutch legislation to make this work public.

Turbulent boundary layers over substrates with streamwise-preferential permeability

Friso H. Hartog ^{1,2,*} Michiel van Nesselrooij ^{1,2} Olaf W. G. van Campenhout ^{1,2}

Ferry F. J. Schrijer ¹ Bas W. van Oudheusden ¹ and Kunal Masania ³

¹*Aerodynamics Group, Faculty of Aerospace Engineering, Delft University of Technology, 2629 HS Delft, The Netherlands*

²*Dimple Aerospace B.V., 2629 HS Delft, The Netherlands*

³*Shaping Matter Lab, Faculty of Aerospace Engineering, Delft University of Technology, 2629 HS Delft, The Netherlands*



(Received 9 May 2024; accepted 26 September 2024; published 4 November 2024)

Recent numerical studies have suggested the potential of substrates with streamwise-preferential permeability to reduce drag in turbulent boundary layers. Such a substrate is theorized to facilitate relaxation of the no-slip condition and thereby reduce the skin friction. So far, these beneficial effects have not been demonstrated experimentally yet and therefore the scope of this work is to present this concept in air flow where the substrate geometry satisfies the theoretical permeability requirements for an expected reduction in drag. For this, a three-dimensional-printed structure with anisotropic permeability ($\phi_{xz} = 2.7$, $\phi_{xy} = 3.9$) and small pores ($s \approx 250 \mu\text{m}$), akin to an acoustic liner, was developed. The substrate was investigated using direct force measurements and 2D-2C PIV in the range of $U_\infty \approx 5\text{--}35 \text{ ms}^{-1}$, corresponding to frictional Reynolds numbers of $\text{Re}_\tau \approx 430\text{--}1960$. Results show an increase in drag of $0\% < \Delta C_D < 8\%$ and, while contrasting the model predictions, this agrees with DNS data on structures with similar geometric properties when using the inverse wall-normal Forchheimer coefficient, or inertial permeability, as the equivalent roughness parameter. Hence the present results constitute the first experimental evidence that this is the governing property for the drag behavior of acoustic liners. The absence of the predicted beneficial flow modulation effects is attributed to the investigated substrate not strictly satisfying the theoretical framework assumptions on characteristic length scales. However, to expand beyond this structural limitation, we analytically derive that, for realistic, geometrically resolved cases, this length scale mismatch is unavoidable and thereby render it unfeasible to model the substrate as a continuum for the virtual-origin approach. We expect that translating the abstraction of substrates with streamwise-preferential permeability into physical realisations relevant for practical applications would result in structures very similar to riblets.

DOI: [10.1103/PhysRevFluids.9.114602](https://doi.org/10.1103/PhysRevFluids.9.114602)

I. INTRODUCTION

Reducing turbulent friction drag has received considerable attention given the need for energy savings and CO₂ reductions in aviation. In particular passive techniques through surface manipulations, such as riblets [1–3], superhydrophobic surfaces [4,5], or permeable substrates [6,7], are interesting from an application perspective. Whereas riblets have already been extensively studied

*Contact author: f.h.hartog@tudelft.nl

and superhydrophobic surfaces pertain to use in liquids only, permeable substrates are a relatively new and unexplored terrain in the context of drag reduction. The drag behavior of permeable substrates in turbulent flow is not fully understood and their ability to reduce drag in experimental settings is unconfirmed. Recent promising work on substrates with streamwise-preferential permeability has presented a theoretical framework behind the flow modulation effects and reported drag reduction up to 25% in direct numerical simulations (DNS) [7]. The present work aims to further investigate this potential by taking the approach of the theoretical framework into an experimental context in relation to air flows in particular.

For a long time, the general consensus has been that permeable substrates exhibit drag-increasing behavior in turbulent boundary layers compared to solid, smooth walls. The first endeavors into this topic involved experimental work using sediment, beds of spherical particles, and porous metals as permeable substrates. Several studies found that for turbulent flow, porous surfaces increase the friction factor [8–14]. Velocity profiles over permeable substrates were more turbulent than over impermeable walls, as reflected by a downward shift of the logarithmic region of the wall law [12,13]. Subsequent particle image velocimetry (PIV) measurements revealed that an increase in permeability enhances turbulent fluctuations in the wall-normal velocity component [15,16]. This supported earlier observations that wall permeability enhances momentum flux and consequently Reynolds stresses near the flow-substrate interface, leading to additional energy dissipation [11]. Similar flow behavior was found using direct numerical simulations [17], in which the flow inside the porous wall was modeled as a continuum via a volume-averaged Navier-Stokes approach, to avoid the prohibitive additional computational effort when resolved the pores explicitly. For a highly permeable wall, the overlying turbulence was dominated by relatively large vortical structures, hypothesized to be of Kelvin-Helmholtz (KH) type. This enhanced the exchange of momentum between the bulk flow and the top layer of the porous medium, resulting in an increased Reynolds shear stress and hence higher skin friction. Later studies, both through fully resolved lattice-Boltzmann simulations and PIV experiments, confirmed this hypothesis and found the influence of KH instabilities to become more significant over a permeable layer compared to an equivalent rough wall, resulting in the occurrence of much larger spanwise length scales [18,19].

The exact relationship between flow modulation effects of permeable substrates and their geometrical properties is still a subject of debate. Observed drag increases have been attributed to the permeability (a measure of the ease with which fluids can pass through a porous medium), porosity (a measure of the void spaces in a porous medium), (equivalent) surface roughness, characteristic length scales (often pore size), or a combination of these. Isolating these effects has proven challenging because permeable materials can range widely in structural lay-out, especially when not constrained by specific geometric design parameters, as is often the case with porous foams. Moreover, properties of permeable substrates are often interdependent, such as pore size and permeability. First attempts at uncovering the properties governing the drag increase included a direct comparison between permeable and impermeable surfaces with equivalent surface roughness [12]. The increase in friction due to permeability was experimentally found to be an effect acting separately from, and in addition to, the surface roughness effect. The influence of permeability and porosity was investigated by decoupling the two properties in a DNS study where the flow inside the substrate was modelled as a continuum [20]. Permeability emerged as the key parameter that determined the response of the channel flow to the porous wall, even at low permeability values. The separation of permeability and roughness effect has been further explored and quantified in an extensive experimental parametric study [21]. They argue that for the porous substrates tested, the change in drag follows a roughnesslike increase. Here the equivalent sandgrain roughness k_s includes both roughness and permeability contributions, which can be separated by considering the same substrates with different thickness. However, it is likely that this behavior is dependent on the specific geometry of the permeable substrate, especially if it does not have an isotropic structure. For example, for anisotropic porous substrates with a perforated wall, resembling acoustic liners, recent work involving fully resolved DNS has shown that the drag increase actually scales with the inverse wall-normal Forchheimer coefficient or inertial permeability [22] as roughness parameter. This

diversity in substrate characteristics responsible for observed increases in drag mentioned across the literature suggests that it is not possible to generalize the effects of permeable substrates on the overlying flow.

Challenging the prevailing view, several studies in the past decade have suggested that under certain conditions permeable substrates can realize drag reductions in turbulent boundary layers [6,7,23]. The explicit objective of friction reduction by using permeable substrates was first pursued in numerical studies [6]. The authors took inspiration from friction reductions reported for seal furs in turbulent boundary layers in water [24]. They explored the possibility of using substrates with streamwise-preferential permeability to reduce turbulent skin friction by promoting relaxation of the no-slip condition at the surface. This follows the physical working mechanism of superhydrophobic surfaces [4,5], and abstracted working mechanism of riblets if viewed from the perspective of the virtual origin framework [3]. A coherent theoretical framework was proposed, linking the substrate viscous permeability, or Darcy coefficient, to slip lengths in all three principal directions, and a subsequent predicted reduction in turbulent friction [7]. This model includes the onset of spanwise-coherent structures associated with a KH-like instability for wall-normal permeabilities above a certain threshold and hence provides an *a priori* method to define the drag-reducing design space in terms of substrate permeability. The model predictions were verified in the same study with results from DNS, showing promising drag reductions up to 25%, for substrates modelled as a continuum with streamwise-preferential permeability and a high anisotropy ratio of $\phi_{xz} = \sqrt{K_x^+}/\sqrt{K_z^+} > 10$. Other DNS results, using a similar continuum approach for modeling the permeable substrate, reported comparable drag reductions of 20% for shallow streamwise-preferential permeable substrates [23]. In these studies, it was not investigated to what extent the simplifications introduced by this modeling approach of the substrate masks potential effects of its geometrical properties on the flow modulation and drag characteristics. However, most recent work using scale-resolved DNS did not find any drag reduction for porous lattices, and suggests that the microstructure at the flow-substrate interface has a significant influence on the flow modulation, which is not accounted for when a continuum-based model is used for the permeable substrate [25].

To date, little experimental work has been performed on the drag characteristics of substrates with streamwise-preferential permeability. No studies have validated the predictive model by Gómez-de Segura and García-Mayoral [7], and no drag reductions have been reported. Moreover, the existing literature offers minimal guidance on the practical design and manufacturing of such substrates. The seal fur studied by Itoh *et al.* [24] has been mentioned as a possible example in nature, a grid of rods parallel to only the streamwise [7] and both the streamwise and spanwise [26] directions has been imagined, experiments with anisotropic permeable substrates using polymer nets have been performed, albeit not with streamwise-preferential permeability specifically [27], and a layered structure composed of corrugated and flat stainless-steel woven-wire-mesh sheets was realized in most recent work [28]. In fact, to the authors knowledge, this latter study is the only experimental work to date wherein the substrate satisfied the permeability requirements for predicted drag reductions. However, none were reported, and similarly to prior DNS findings [7] it is suggested that the observed drag increase is controlled by the wall-normal permeability $\sqrt{K_y^+}$. More suitable for tailored designs, three-dimensionally (3D) printed porous lattices with streamwise-preferential permeability have been used for experiments in water flows [29]. Unfortunately, these structures had too high a wall-normal permeability to test the validity of drag reduction predictions, and indeed an increase in friction was found. In line with the drag increase, energetic footprints of spanwise-coherent structures linked to a KH-like instability were observed. Also, the authors indicated the presence of a streamwise slip length related to the streamwise permeability of the substrate. Although no drag reduction was measured, both observations were in line with other aspects of the theoretical framework and observations from DNS [7]. This shows the suitability of 3D printing as a method to create permeable substrates with streamwise-preferential permeability for flow modulation purposes. The remaining challenge is to design and create a suitable substrate

with appropriate permeability values that could lead to the desired flow modulation effects and drag-reducing characteristics.

In the present work, we study the flow modulation effects and drag characteristics of substrates with streamwise-preferential permeability. A permeable structure was designed and 3D printed, and on measurement, its permeability values were found to satisfy the criteria for predicted drag reductions according to the theoretical model by Gómez-de Segura and García-Mayoral [7]. It was subsequently investigated in wind tunnel experiments using direct force measurements and PIV measurements. These results are compared against predictions from the theoretical model and correlated with substrate characteristics to identify a governing parameter driving the observed drag behavior. In view of the observed discrepancies between model predictions and experimental results, we make a critical assessment of the applicability of the theoretical framework to our experimental study specifically, and physical circumstances in general, taking the main framework assumptions and potential limitations into account.

The outline of this paper is as follows: Section II first summarizes the aforementioned theoretical framework before it covers the experimental methodology of the present work, giving details of the permeable substrates, wind tunnel facility, and experimental techniques. Then, Sec. III presents the experimental results, including the drag characteristics and wall-normal profiles. Subsequently, Sec. IV discusses the results in relation to facilitating slip, drag behavior, and the application of the theoretical framework in experimental settings. Finally, Sec. V concludes on this work.

II. METHODOLOGY

A. The theoretical framework linking substrate permeability to predicted drag reductions

The theoretical framework proposed by Gómez-de Segura and García-Mayoral [7] enables drag reduction predictions for substrates with streamwise-preferential permeability based on the following modeling assumptions: (1) The permeable substrate is modelled as a continuum with constant permeability values; (2) the substrate characteristic length scales (pore size) are assumed “much” smaller than the smallest turbulence length scale and taken infinitesimally small; and (3) the effect of pressure drag within the permeable substrate is deemed negligible. Linking the substrate permeability to predicted drag reduction rests on the following four building blocks:

(1) *Surface manipulations and ΔU^+* . The only noticeable effect of surface manipulation on the flow sufficiently far away from the wall is the modification of the intercept of the logarithmic law (expressed as ΔU^+), while both the von Kármán constant and wake function remain unaltered [30]. Here the superscript + indicates the conventional viscous-unit scaling employing the friction velocity u_τ and the kinematic viscosity ν . $\Delta U^+ > 0$ indicates an upward shift of the logarithmic region which corresponds to a reduction in drag [since $C_f = 2(U_\infty^+)^{-2}$], and $\Delta U^+ < 0$ vice versa.

(2) *Virtual origins and slip length*. Surface manipulations with small characteristic length scales can lead to different perceived wall locations for the mean flow and quasi-streamwise vortices, giving different virtual origins for the corresponding velocity profiles, effectively “pushing turbulence away from the wall” [6]. Since the velocity profile near the wall is essentially linear, this concept can be expressed through a Navier slip condition. For riblets, superhydrophobic surfaces, and permeable substrates, the resulting drag reduction (expressed as ΔU^+) is proportional to the difference in streamwise and spanwise slip length: $\Delta U^+ \propto (\ell_x^+ - \ell_z^+)$ [31].

(3) *From permeability to slip length*. Solving Brinkman’s equation (describing flow through a permeable medium) analytically in response to an overlying homogeneous shear for highly connected, deep ($h^+ > \sqrt{K_i^+}$) substrates, leads to a direct relationship between the slip length and permeability, i.e., $\ell_i^+ = \sqrt{K_i^+}$ [6]. Here h is the substrate thickness or depth, and the subscript i denotes any of the three principal directions x , y , or z respectively. Subsequently, the resulting drag reduction can be expressed as a linear relationship: $\Delta U^+ \propto (\sqrt{K_x^+} - \sqrt{K_z^+})$.

(4) *Drag degradation effects*. For too large wall-normal permeability, KH-like instabilities result in the emergence of spanwise coherent structures and the linear drag reduction trend breaks down.

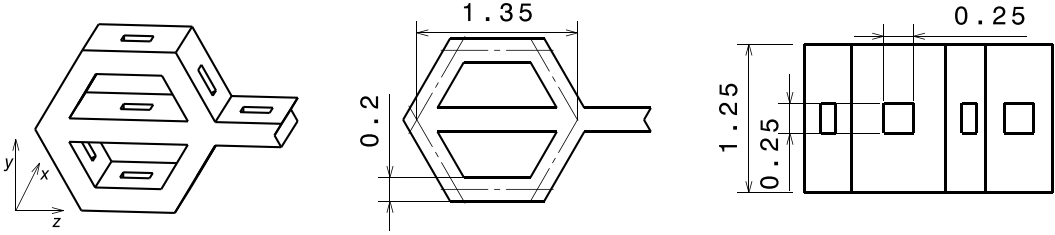


FIG. 1. Unit cell design. From left to right: Isometric view, front view (yz plane) and top view (xz plane). Axis system in isometric view represents principal permeability directions, K_x , K_y , and K_z , corresponding to streamwise, wall-normal, and spanwise directions in wind tunnel experiments. Dimensions in mm.

Through linear stability analysis this was predicted to set in at $\sqrt{K_y^+} \approx 1$ [31], but later DNS results showed that this occurs already for $\sqrt{K_y^+} > 0.38$ [7]. This discrepancy is attributed to the difference between deep and shallow substrates, where the latter might delay the onset of KH-rollers to higher values of $\sqrt{K_y^+}$ due to the wall-blocking effect.

Following this framework results in three main criteria for permeable substrates to realize drag reductions, namely: (1) a high anisotropy ratio ϕ_{xz} to achieve a large difference in streamwise and spanwise slip; (2) a low wall-normal permeability $\sqrt{K_y^+}$ to prevent the occurrence of KH-rollers; and (3) small length scales (i.e., pore size and wall thickness) to satisfy the assumption of having substrate characteristic length scales, or “pores,” that “are much smaller than any near-wall turbulent length scale” [7]. Unfortunately this scale separation criterion is not further worked out nor quantified in the theoretical framework. The following section covers how these criteria were translated into design requirements and resulted in the permeable substrate investigated in the present study. The implications of the scale separation assumption on the design of permeable substrates in an experimental context is further discussed in Sec. IV C.

B. Permeable substrate design

Designing and creating a suitable permeable substrate requires a careful balancing between adhering to the criteria outlined in the previous section on the one hand, and considering manufacturing feasibility on the other. Stereolithography 3D printing, using a Prusa SL1 and Prusament Tough Resin, was chosen as manufacturing method due to its suitability for tailored designs of homogeneous structures with repeating unit cells and small geometrical features. Conceptualising the design based on the desired permeability characteristics gives a porous structure that is well connected in streamwise direction, and poorly connected, but not impermeable, in wall-normal and spanwise directions. Accounting for the length scale criterion further drives the repeating unit cells to be as small as possible. In practice, limitations in printing resolution and structural integrity defined the lower bounds on pore size ($\approx 250 \mu\text{m}$) and wall thickness ($\approx 200 \mu\text{m}$) within the substrate. These bounds were found through an iterative process of printing samples with increasingly smaller geometrical features and experimentally characterising their permeability, up to the point where the structure would either be too soft, or contain a significant amount of permanently clogged pores.

The resultant permeable substrate investigated in this study was a repeating perforated half-hexagon unit cell (Fig. 1) embedded in a 3.8-mm-thick structure (Fig. 2). It resembles an acoustic liner, in that it has a perforated top plate and backing-cavity structure. The prints were examined under a Keyence One-Shot 3D VR-5200 microscope. The average wall-normal pore geometry was close to the design with dimensions of $234 \pm 13 \mu\text{m} \times 290 \pm 34 \mu\text{m}$. The observed deviations were expected, given that the design has feature sizes at the limit of the printer’s resolution. Roughness analysis was performed on the solid inter-pore surface along the streamwise direction. Both the absolute arithmetic mean of the roughness profile (R_a) and roughness bandwidth (mean

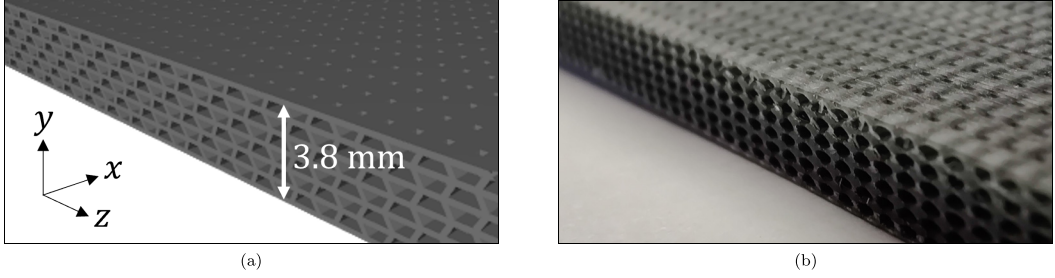


FIG. 2. Three-dimensionally printed sample with streamwise-preferential permeability. $h/s \approx 15.2$, $h/\sqrt{K_x} \approx 64.3$, and $h/\sqrt{K_y} \approx 251$, where h and s refer to the substrate thickness and pore size respectively. (a) Schematic render. Axis system represents streamwise, wall-normal, and spanwise directions in wind tunnel experiments. (b) Physical realisation.

peak-to-peak) were found to be small enough ($k_s^+ < 1$) to ensure hydrodynamic smoothness, i.e., $0 < k_s^+ < 5$ [32], at all tested flow conditions. Here k_s is the roughness length scale. However, when considering the pore size of $s \approx 250 \mu\text{m}$ as characteristic length scale for roughness elements, roughness effects cannot be excluded (see Table I) [21]. The implications of this are discussed in Sec. IV B. The surface porosity (i.e., the pore coverage of the surface area) is $\epsilon_{\text{surface}} \approx 3.7\%$, and the porosity of the entire structure is $\epsilon \approx 52\%$. Permeability in the three principal directions was characterized by fitting the compressible Forchheimer's equation [33] to the pressure drop and volumetric flow rate data obtained with the experimental setup as described in Ref. [34] and found to be $K_x = (35 \pm 2.5) \times 10^{-10} \text{ m}^2$, $K_y = (2.3 \pm 0.3) \times 10^{-10} \text{ m}^2$, and $K_z = (4.7 \pm 0.2) \times 10^{-10} \text{ m}^2$. The corresponding viscous-scaled anisotropy ratios are $\phi_{xz} = 2.7$ and $\phi_{xy} = 3.9$. In the range of tested flow conditions, these values cover the viscous-scaled permeability design space (see Table I), that includes both the linear drag reduction regime (with a maximum predicted drag reduction of 6.4%) and the point of breakdown with the emergence of KH-rollers (at $U_\infty \approx 8 \text{ ms}^{-1}$), according to characteristics derived from Ref. [7]. In conclusion, the design and manufacturing approach resulted in a substrate that satisfies the permeability requirements to test the drag-reducing flow modulation hypotheses.

C. Wind tunnel and test section

Wind tunnel experiments were performed in an open-circuit wind tunnel. It can operate at a freestream velocity of up to approximately 35 ms^{-1} , with a freestream turbulence intensity of approximately 0.7%. A velocity range of $5\text{--}35 \text{ ms}^{-1}$ was taken in this study. A schematic of the experimental setup including the streamwise locations of the drag balance and PIV field of views is shown in Fig. 3. Measurements were performed in a test section with a $400 \text{ mm} \times 400 \text{ mm}$ cross section. A turbulent boundary layer is created on a plate with an elliptical leading edge with a carborundum strip, 600 mm upstream of the investigated surface, which is either the permeable substrate or its smooth counterpart. Similar experiments from previous studies suggest that boundary layer development over porous substrates requires a streamwise distance of approximately $40h$ [35],

TABLE I. Viscous-scaled substrate characteristics for the velocities tested in the PIV measurements.

$U_\infty (\text{ms}^{-1})$	5	10	20	30
$\sqrt{K_x^+}, \sqrt{K_y^+}, \sqrt{K_z^+} (-)$	0.90, 0.23, 0.33	1.76, 0.45, 0.64	3.34, 0.86, 1.23	4.84, 1.24, 1.78
$h^+ (-)$	58	113	215	311
$s^+ (-)$	3.8	7.4	14.1	20.5

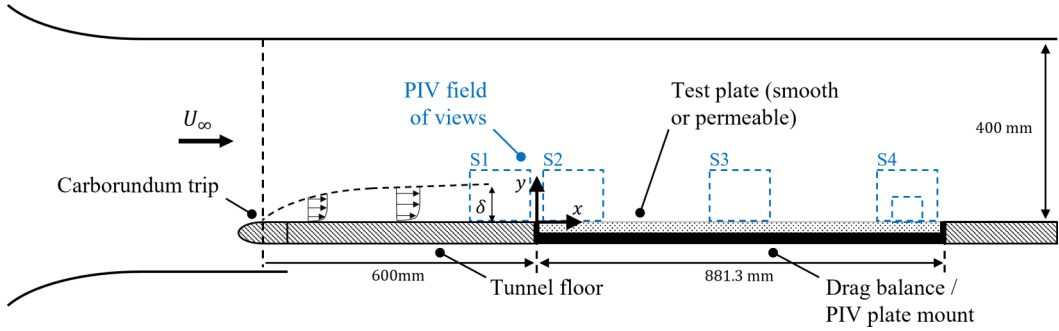


FIG. 3. Schematic of the experimental setup in the wind tunnel. U_∞ = freestream velocity. δ = boundary layer thickness. S1 to S4 indicate “Stations” for the different PIV field of views, having their centers at streamwise locations (x) of -35 , 76 , 454 , and 816 mm with respect to the test plate leading edge, respectively.

which would translate to approximately 17% of the streamwise extent of the permeable substrate in the present study. On measurement, it was verified that the boundary layer had adapted to the permeable substrate between $20h$ (S2 in Fig. 3) and $120h$ (S3), or between 9% and 52% of its streamwise extent.

D. Direct force measurements

Direct force measurements were performed with a drag balance that has been designed especially for thin, flat plates of fixed dimensions (length \times width \times thickness: $881.3 \text{ mm} \times 366.1 \text{ mm} \times 5.0 \text{ mm}$). Further specifications of the apparatus can be found in a previous publication [36]. It can perform calibrated force measurements in flow velocities up to sonic speeds with corrections for pressure forces acting on the streamwise-facing surfaces within the cavities between the connector tray holding the test plate and the rest of the device. It is capable of measuring differences in drag on the order of percents with a 95% confidence interval of typically less than 0.5%–1.0%. The balance and test plate are mounted flush with the wind tunnel bottom wall. This setup has been validated for passive flow control methods, specifically with riblets [36] and dimples [37].

The test plate with the permeable substrate, from hereon referred to as the permeable plate, has a solid aluminium bottom and rim around the perimeter of the permeable material to prevent flow leaking out of the test plate. It was compared against a smooth aluminium reference plate also used in other studies [36,37]. Three measurements on different dates were performed: two for the full range of $U_\infty \approx 5\text{--}35 \text{ ms}^{-1}$ and one for a low-velocity range of $U_\infty \approx 5\text{--}11 \text{ ms}^{-1}$. In every measurement, the permeable plate was measured in both streamwise orientations, i.e., a predetermined “regular” orientation, and a “reversed” orientation where the permeable plate was rotated 180° around the y axis.

E. Particle image velocimetry

2D-2C PIV was performed in the streamwise wall-normal xy plane located at the test plate spanwise center-line ($z = 0$). Details on settings, parameters, and resulting properties pertaining to the PIV measurements are given in Table II. An sCMOS CLHS camera (LaVision GmbH), with a pixel size of $6 \mu\text{m}$ and sensor size of $2560 \text{ px} \times 2160 \text{ px}$, was mounted on a rail to traverse parallel to the streamwise direction and measure at four different streamwise locations (shown in Fig. 3). An AF Micro Nikkor 105 mm lens was used at apertures of $f/8$ and $f/16$ for the full BL and zoomed-in views, respectively. Tracer particles were generated from a water-glycol mixture by a SAFEX Fog 2010+ smoke generator and illuminated using a double-pulsed ND:Yag Evergreen 200 (Quantel Laser) with a 15- mJ/pulse power setting. The laser beam, with a wavelength of 532 nm, was formed into a sheet of approximately 1.5–2.0 mm thickness via a set of spherical and cylindrical

TABLE II. Settings, parameters, and properties of the PIV measurements. Δt = image separation time, BL = boundary layer, SE = standard error, FOV = field of view, and ov = overlap.

General				
Seeding	1 μm water-glycol droplets			
Illumination	ND:YAG, 532 nm, 2×200 mJ at 75% power setting			
Camera	sCMOS, 2560 px \times 2160 px sensor size, 6 μm pixel size, 16 bits			
Lens focal length (mm)	105			
Recordings per measurement (no.)	600			
Acquisition rate (Hz)	15			
Exposure time (μs)	10			
Velocity specific				
U_∞ (ms^{-1})	5	10	20	30
Δt (μs), full BL/zoomed-in view	69/52.2	34.5/26.1	17.2/13.1	11.5/8.7
\bar{u} SE (%), smooth/permeable	0.028/0.037	0.023/0.028	0.019/0.032	0.019/0.031
$\bar{u} _{y^+ < 30}$ SE (%), smooth/permeable	0.16/0.27	0.17/0.31	0.19/0.81	0.22/1.1
u_{rms} and v_{rms} SE (%), smooth/permeable	0.23/0.23	0.23/0.23	0.23/0.23	0.23/0.23
$\overline{u'v'}$ SE (%), smooth/permeable	0.81/0.81	0.83/0.84	0.85/0.86	0.87/0.88
FOV specific				
FOV type	Full BL view		Zoomed-in view	
FOV, $w \times h$ (mm \times mm)	43.5 \times 36.7		22.3 \times 18.8	
Locations	S1, S2, S3, S4		S4	
Resolution (px per mm)	58		115	
Particle displacement (px per image pair)	20		30	
Aperture (–)	$f/8$		$f/16$	
Correlation method specific				
Correlation method	Cross-correlation		Sum of correlation	
Initial pass window	96 \times 96, elliptical 2:1, 75% ov		16 \times 16, square, 75% ov	
Final pass window	16 \times 16, elliptical 2:1, 75% ov		4 \times 4, circular, 75% ov	
Final passes (no.)	2		2	
Vector pitch (μm), full BL/zoomed-in view	68/34.8		17/8.7	
Δy^+ (–) at 30 ms^{-1} , full BL/zoomed-in view	5.6/2.9		1.4/0.7	

lenses. The camera and laser were controlled from DaVis 10 software and timed and triggered via a programmable timing unit from LaVision GmbH.

Processing of the PIV data was performed using LaVision DaVis 10 and MATLAB software. Raw images were preprocessed with a Butterworth high-pass filter (filter length of seven images). Two different correlation methods were used: cross-correlation and sum of correlation. The former allows for quantifying the turbulence statistics, while the latter provides four times more resolution in the mean velocity wall-normal profiles, and which was used for investigating the mean flow behavior in the inner layer. Vector fields were exported from DaVis and further processed with MATLAB. Wall-normal profiles and integral properties such as boundary layer thickness were created and calculated respectively through spatial averaging along x in the entire FOV, in view of the streamwise homogeneity of the flow. The uncertainty in the wall-normal profiles was quantified following the method from Ref. [38] based on 600 image pairs and 160 uncorrelated samples per image pair, i.e., every fourth vector element in the streamwise direction to account for the 75% overlap in interrogation window, and found to be within 1% for all flow statistics and at all freestream velocities investigated (see Table II). The friction velocity (u_τ) was estimated with a

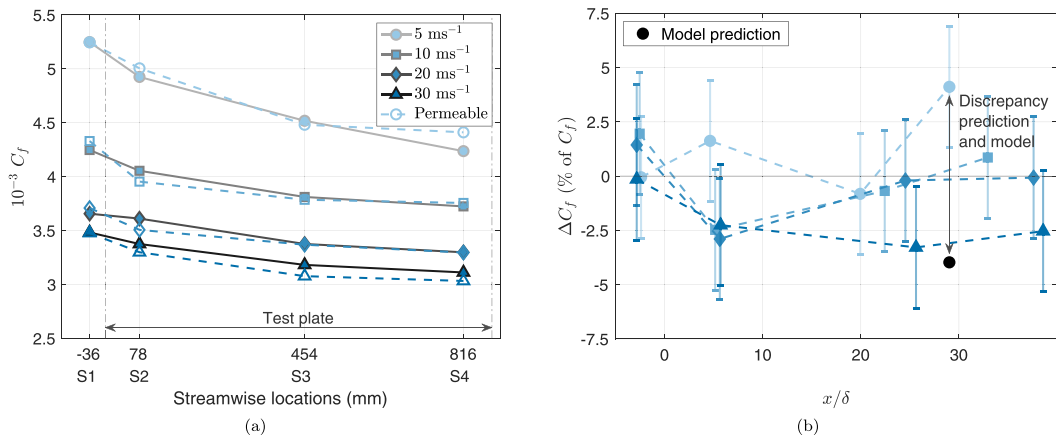


FIG. 4. Development of friction coefficient (C_f) over the test plate for different velocities. Data obtained from PIV experiments (via fitted u_τ). (a) Absolute values for reference and permeable plate for different absolute streamwise locations; S1, etc., indicate the position of the different FOVs, see Fig. 3. (b) Percentage difference of permeable with respect to reference plate for normalized streamwise locations x/δ . Error bars are defined as $\pm 2.8\%$ in ΔC_f .

boundary layer fitting routine adapted from Ref. [39], whom reported maximum uncertainties in estimates on u_τ of 0.6%.

III. RESULTS

A. Drag

Figure 4 shows the development of the friction coefficient (C_f) along the streamwise direction. Here C_f is defined as $C_f = 2(u_\tau/U_\infty)^2$ using data obtained from the PIV measurements. It follows the expected Reynolds number trend for turbulent boundary layers, with decreasing values of C_f for increasing velocities and increasing development length. Also, the difference in friction coefficient (ΔC_f) of the permeable plate with respect to the reference smooth plate is shown, including the value predicted via the theoretical framework. The latter could only be done for $U_\infty = 5 \text{ ms}^{-1}$, as the higher velocities yielded viscous-scaled wall-normal permeability values higher than the threshold of $\sqrt{K_y^+} \approx 0.38$ above which the linear drag-reduction regime breaks down (conforming the data in Table I).

The results show a discrepancy between the measured and predicted values of ΔC_f . Moreover, at the most downstream location (Station 4) ΔC_f decreases from most positive to most negative for increasing velocity, a trend opposite to expectations based on the theoretical framework. In general, the results only yield very small differences in C_f between the permeable and reference plates. It is expected that these differences fall within the uncertainty that results from the fitting procedure for u_τ . Uncertainties in u_τ of 0.6% (according to Ref. [39]) would translate into relative uncertainties in C_f of 1.2%, and absolute uncertainties in ΔC_f (when expressed in percentage difference) of 1.7%. For studies on turbulent boundary layers over permeable substrates specifically, worst-case uncertainties in u_τ of up to 5% have been reported [21]. An estimate for the uncertainty in this study can be taken from the observed difference in C_f between the permeable plate and smooth plate measurements upstream of the test plate leading edge at Station 1, where one would expect identical values. The maximum observed difference here of approximately 2% is taken as the uncertainty bound on C_f , resulting in an absolute uncertainty bound on ΔC_f of approximately $\pm 2.8\%$. The lack of trends in the data and the observation that the majority of the data points lie within the estimated

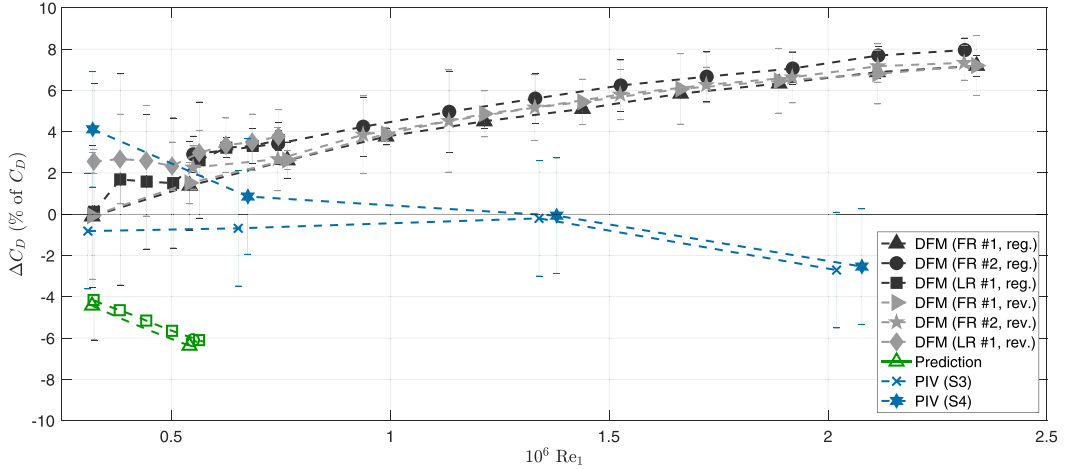


FIG. 5. Drag change for permeable surface with respect to reference smooth wall. Red: Prediction based on theoretical model. Black and gray: Results from direct force measurements. Blue: Estimation based on ΔC_f (via u_τ) from PIV experiments. DFM: Direct force measurements. FR: Full velocity range. LR: Low-velocity range. Reg.: Regular orientation. Rev.: Reversed orientation. S3 and S4 denote Stations 3 and 4 from the PIV experiments. Error bars are defined as 95% confidence interval for direct force measurements, and $\pm 2.8\%$ in ΔC_f for estimates from PIV.

uncertainty bounds, therefore render the data on ΔC_f obtained via the PIV measurements in itself inconclusive regarding a potential drag reduction and validity of the theoretical framework.

Figure 5 presents the drag results as obtained from the direct force measurements. It shows the difference in drag (ΔC_D) of the permeable plate with respect to the smooth plate. It also contains the results from the PIV experiments for Stations 3 and 4, where the drag difference corresponds to the difference in friction (ΔC_f) as obtained via u_τ from fitting viscous-scaled velocity profiles [same values as in Fig. 4(a)]. The theoretical model drag reduction predictions are computed with respect to the drag coefficient from the direct force measurements for the reference smooth plate (C_{D_0}), using the corresponding flow conditions to determine the viscous length scale $\delta_v (= \nu/u_\tau)$ required for expressing the permeabilities in viscous units. Experimental data and predictions are plotted with identical marker shapes per corresponding reference measurement. Predictions continue with increasing unit Reynolds number (Re_1 , from hereon simplified as Re) until the point of breakdown, above which $\sqrt{K_y^+} > 0.38$ and the model cannot predict drag reduction values.

The direct force measurement results show a slight to moderate drag increase that grows with increasing Re , up to a maximum of 8%. The results show no particular dependence on measurement date, nor plate orientation. In general, there is good repeatability of the results with an error bound of approximately $\pm 1.5\%$ of C_D . For $Re < 0.5 \times 10^6$, larger discrepancies between different measurements can be observed, with an uncertainty bound of $\pm 6\%$ of C_D at the lowest Re . This can be attributed to the smaller absolute forces and consequent larger relative measurement error. Nevertheless, there is a noticeable difference between the experimental data and the predictions, both in values and trend. This indicates that the permeable plate does not reduce drag as would be expected based on its permeability values alone, following the theoretical framework.

The results from the direct force measurements and the PIV experiments exhibit significant differences which grow with increasing Re or velocity. A first explanation could be the uncertainty in the fitting of u_τ , which might be larger than anticipated here. Uncertainties on u_τ values in the order of 5% (as observed for porous substrates in Ref. [21]) would translate to uncertainties in ΔC_f in the order of 14%, putting the direct force measurement results within the error margin of the PIV results. However, this fails to explain the growing difference with increasing Re . A more

encompassing cause would be the occurrence of pressure drag within the permeable substrate. This effect is likely to increase with increasing Re , and is captured in direct force measurements but omitted when inferring the drag from fitted velocity profiles. Moreover, this phenomenon and its contribution to the integral drag are omitted in the theoretical framework and numerical studies modeling permeable substrates as a continuum. Consequently, this observation prompted a more detailed examination of the factors potentially driving the significant and consistent drag increase in the direct force measurements, and therefore these results are further discussed in Sec. IV B.

B. Wall-normal profiles: Mean velocity and turbulence statistics

Figure 6 shows the wall-normal profiles, specifically viscous-scaled mean streamwise velocity, streamwise and wall-normal velocity fluctuations, and Reynolds shear stress, obtained from the PIV measurements at $U_\infty = 10$ and 30 ms^{-1} at Station 4, the location with the longest boundary layer development length. All profiles are scaled with the smooth wall friction velocity u_{τ_0} to highlight absolute differences and to exclude uncertainties in u_τ . The mean velocity profile is based on the sum-of-correlation data, the other statistics on the cross-correlation data, hence the difference in vector pitch between the profiles. In general, all profiles have similar shapes when comparing the permeable and smooth plate cases and the latter agrees well with the reference DNS data [40]. Deviation from the reference DNS data is most significant for the wall-normal velocity fluctuations (and therefore the Reynolds shear stresses) due to spatial averaging effects: turbulent flow structures with length scales smaller than the cross-correlation window size are not resolved, hence their energetic content is not captured. Similar observations were shared in Ref. [29]. Uncertainty is represented by error bars that are included in some of the data zooms and which correspond to ± 2 SE where SE is the standard error (corresponding to Table II).

Comparing the mean velocity profile of the permeable substrate to the smooth wall shows little differences between the two. Notably, no slip can be observed for the permeable surface: the velocity profile near the wall follows the linear relationship $u^+ = y^+$ and does not show an increased value of u^+ , indicating the absence of an additional slip velocity. This is in contrast to what is predicted by the theoretical model (dash-dotted lines in the inner layer following $u^+ = y^+ + \sqrt{K_x^+}$). Also, it can be observed that in the inner layer ($y^+ < 5$), the experimental data (both smooth and permeable) lies below the linear profile ($u^+ = y^+$) and reference DNS data, especially for $U_\infty = 30 \text{ ms}^{-1}$. This is attributed to a shortcoming in the optical configuration used in the PIV experiments. The camera was installed such that the optical axis was above (and hence not aligned horizontally with) the test plate surface. Hence, for highly zoomed-in views, averaging effects take place because of the height difference along the intersection of the downward-angled optical path within the laser sheet. For the same physical setup, these averaging effects become more pronounced with increasing flow velocity and corresponding decreasing viscous length scale. The affected region has been indicated in Fig. 6 with red shading. The impact of these averaging effects has been confirmed by artificially introducing these effects to a theoretical viscous-scaled velocity profile and finding good overlap with the obtained experimental data. Consequently, this deviation in the experimental mean velocity data is considered to not be related to the flow behavior, but rather to the experimental setup.

For the turbulence statistics, more apparent, but still small, differences between the smooth wall and permeable substrate can be observed. The wall-normal velocity fluctuations show a small increase in the inner layer ($y^+ < 30$) at $U_\infty = 10 \text{ ms}^{-1}$, and a more pronounced increase at $U_\infty = 30 \text{ ms}^{-1}$. This larger increase is attributed to the increase in viscous-scaled wall-normal permeability, which eases the exchange of fluid momentum across the flow-substrate interface. The streamwise velocity fluctuations remain largely unaffected for the majority of the boundary layer and hence the increase in Reynolds shear stress is mainly attributed to the increase in wall-normal velocity fluctuations. These findings were also present at the other streamwise locations (not shown here) and are in line with earlier findings for turbulent flows over permeable walls [7,16,17,41]. Counter to these observations is the slight decrease in the wall-normal velocity fluctuations and

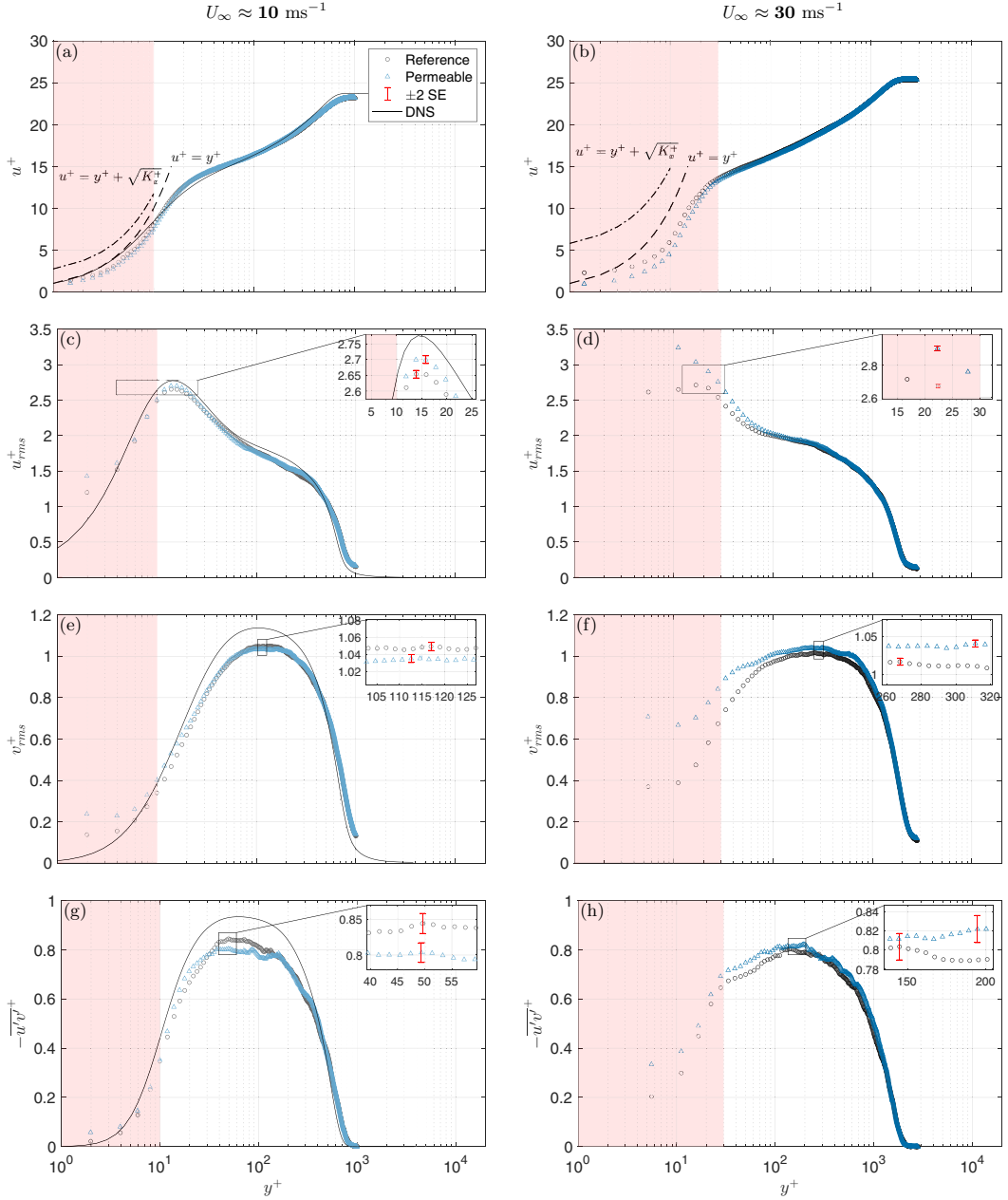


FIG. 6. Wall-normal profiles at Station 4, normalized with u_{τ_0} . [(a), (c), (e), and (g)] $U_\infty \approx 10 \text{ ms}^{-1}$, $Re_\tau \approx 720$ and 720 and $Re_\theta \approx 1920$ and 1880 for smooth wall and permeable surface respectively, $\sqrt{K_x^+} \approx 1.76$, $\sqrt{K_y^+} \approx 0.45$. DNS data for $Re_\tau \approx 670$ and $Re_\theta \approx 2000$ from Schlatter and Örlü [40]. [(b), (d), (f), and (h)] $U_\infty \approx 30 \text{ ms}^{-1}$, $Re_\tau \approx 1740$ and 1710 and $Re_\theta \approx 4890$ and 4920 for smooth wall and permeable surface, respectively, $\sqrt{K_x^+} \approx 4.84$, $\sqrt{K_y^+} \approx 1.24$. [(a) and (b)] Mean velocity (u^+). [(c) and (d)] Streamwise velocity fluctuations (u_{rms}^+). [(e) and (f)] Wall-normal velocity fluctuations (v_{rms}^+). [(g) and (h)] Reynolds shear stress ($-\overline{uv}^+$).

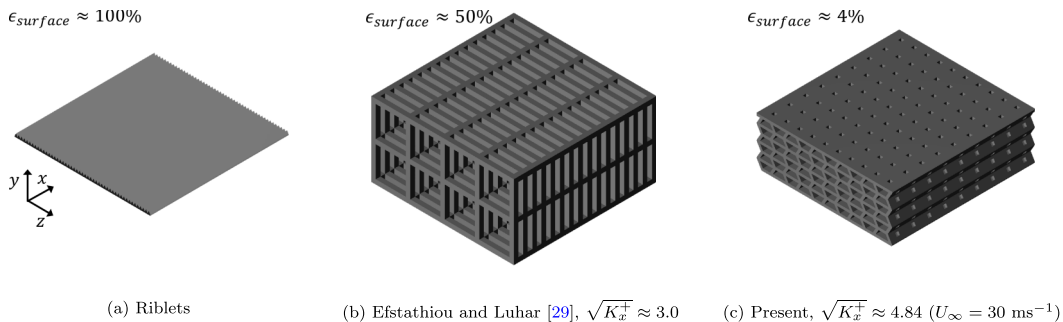


FIG. 7. Isometric view renders of different surfaces. $\epsilon_{\text{surface}}$ = nonsolid wall surface area at interface, expressed in a percentage of total surface area in xz plane at flow-surface interface. Renders at same scale, with $w \times l \approx 11 \times 11 \text{ mm}$.

Reynolds shear stress for $U_\infty = 10 \text{ ms}^{-1}$ occurring in the region $30 < y^+ < 150$ in particular. It is hypothesized that the permeable substrate reduces the characteristic turbulent length scales responsible for the wall-normal velocity fluctuations in the logarithmic layer through mixing, further masking their energetic content within the cross-correlation interrogation window. This effect could obfuscate a smaller increase in wall-normal velocity fluctuations for low viscous-scaled wall-normal permeabilities and disappear at higher velocities when the prevalence of fluid momentum exchange at the flow-substrate interface increases. Although the observed difference is statistically significant, it is small and could potentially be attributed to measurement uncertainties not included in the theoretical error estimation.

IV. DISCUSSION

A. The absence of streamwise slip

Gómez-de Segura and García-Mayoral [7] derived that a permeable substrate provides a streamwise slip related to its permeability via $\ell_x^+ \approx \sqrt{K_x^+}$ and verified this relationship with DNS results. Soon thereafter, Efstathiou and Luhar [29] realized a substrate with streamwise-preferential permeability in an experimental setting, which was able to facilitate streamwise slip in accordance with this relation. However, the substrate had a wall-normal permeability of $\sqrt{K_y^+} \approx 1.1$, too high to validate the theoretical model predictions on drag reduction, and lead to an increase in friction. The values for the streamwise permeability were similar to those in the present study. However, in the present study, no indications of streamwise slip were observed. This discrepancy can likely be attributed to the significantly lower surface porosity ($\epsilon_{\text{surface}}$, i.e., open pore area relative to the entire surface area) in the present study. Figure 7 shows three surface configurations and their ratio of nonsolid area to total area at the surface plane. While the configuration of Efstathiou and Luhar [29] has nearly 50% of the surface plane nonsolid, this value is an order of magnitude lower at approximately 4% in the present study. The majority of the surface therefore imposes a strict no-slip condition on the free flow. Although the substrate in the present study has a sufficiently high streamwise permeability to allow for a measurable streamwise slip based on the continuum approach from the theoretical framework, it physically does not allow for such slip over the majority of the surface. A similar observation was made from the scale-resolved DNS by Habibi Khorasani *et al.* [25], where none of the nine investigated substrates allowed for the development of any significant slip velocity at their surfaces. This illustrates the challenge of providing enough free surface area to facilitate streamwise slip on the one hand, while simultaneously limiting wall-normal permeability. Taking these two requirements to the limit, one can imagine ending up with a structure very similar to riblets; these microscopic structures allow significant streamwise slip when viewed from the

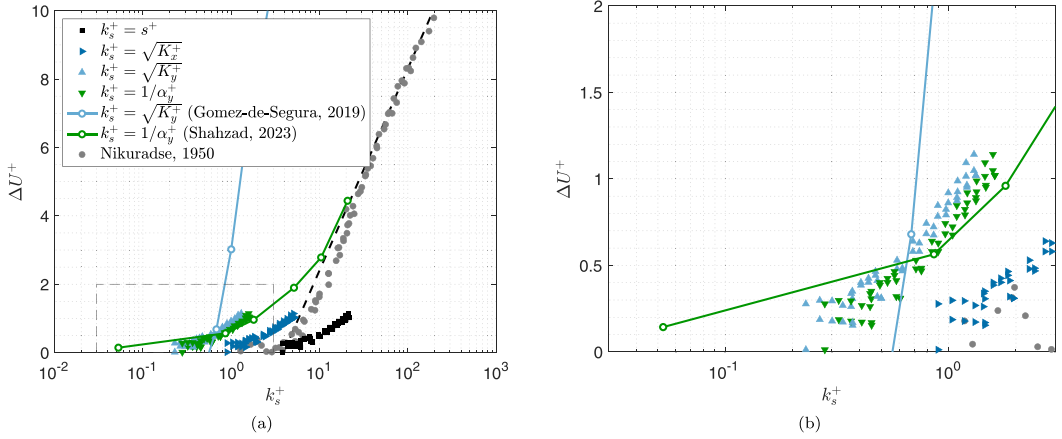


FIG. 8. Change in drag, expressed as ΔU^+ , as function of equivalent roughness (k_s^+). Experimental data plotted for different approaches to define k_s^+ and compared against sandgrain roughness data from Nikuradse [32]. The dashed line indicates the fully rough asymptote $\kappa^{-1} \ln(k_s^+) - 3.5$ with $\kappa = 0.39$. (a) Full view and (b) zoomed-in view (for dashed box in full view).

perspective of the virtual-origin framework, and can be considered impermeable in the wall-normal direction.

B. The increase in drag

The increase in drag for permeable materials has been attributed to different factors, such as the occurrence of KH-rollers at wall-normal permeabilities above a certain threshold value for anisotropic permeable substrates modelled as a continuum [7] or realized as 3D-printed [29] or woven-wire-mesh [28] lattice, a combination of permeability and pore size for isotropic porous foams [21], and the wall-normal Forchheimer coefficient (inertial permeability) α_y for perforated plates resembling acoustic liners [22]. The permeable substrate in the present study resembles the configurations investigated in these studies on different aspects. In terms of viscous-scaled streamwise-preferential permeability values, it is similar to cases A1-A8 studied by Gómez-de Segura and García-Mayoral [7], which formed the basis of the present study. For physical pore size, substrate thickness, and (streamwise) permeability, it is similar to the thin, 90 ppi porous substrate case studied by Esteban *et al.* [21], albeit with an order of magnitude lower wall-normal permeability. In terms of geometrical design, it resembles an acoustic liner as being a perforated plate with connected back-cavities in streamwise direction, and hence is close to case $L-L_3$ studied by Shahzad *et al.* [22], with similar pore coverage of the surface, viscous-scaled pore size, and ratio of pore size to plate thickness. Consequently, the increase in drag observed in the present study is further analysed in comparison to these references to uncover the parameter most likely responsible for the drag behavior.

Figure 8 shows the change in drag observed in the current study, expressed as ΔU^+ , using different approaches to define the equivalent roughness k_s^+ . Herein, $\Delta U^+ = \sqrt{\frac{2}{C_D}} - \sqrt{\frac{2}{C_{D0}}}$, where C_D and C_{D0} are the drag for the permeable surface and reference smooth wall respectively, obtained from the direct force measurements. No experimental data from Esteban *et al.* [21] has been included as the authors have not yet put forward how to isolate the roughness effect *a priori*, prohibiting the combining of the permeability and roughness effects into an equivalent roughness for the present study. None of the approaches show a match with the equivalent sandgrain roughness data from Nikuradse [32]. The pore size approach ($k_s^+ = s^+$) underestimates the drag increase, likely due to the scarce pore coverage of the surface. A better match might be expected for a configuration with more

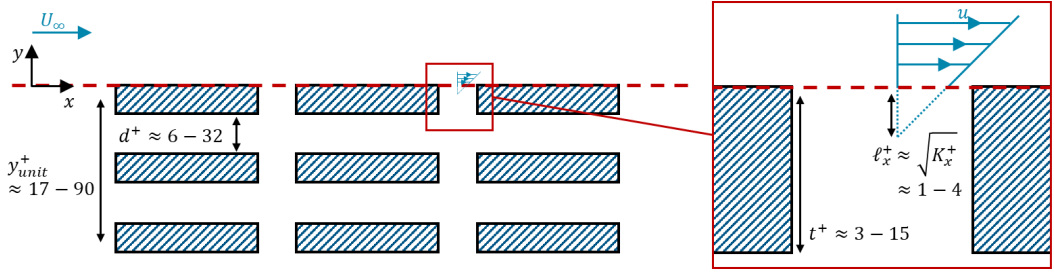


FIG. 9. Schematic of substrate in the present study, including substrate length scales and expected velocity profile penetration depth. Range in values account for different tested freestream velocities ($U_\infty = 5\text{--}30\text{ ms}^{-1}$).

pores of the same size. The wall-normal permeability approach ($k_s^+ = \sqrt{K_y^+}$) does show the same qualitative behavior as previous studies [7,28,29] in that a larger wall-normal permeability correlates with a larger increase in drag. However, it shows no agreement with the DNS data from Gómez-de Segura and García-Mayoral [7], for which the drag increase at similar permeability values (above $\sqrt{K_y^+} > 0.6$) is much larger. It was not possible for us to observe spanwise-coherent rollers from KH-instabilities due to the insufficient resolution in the PIV measurements. Nevertheless, it is deemed unlikely that such KH-rollers have formed in the present study, again due to the scarce pore coverage of the surface, allowing for limited occurrence of inflectional instabilities in the boundary layer profile near the wall. Most notably however, the wall-normal Forchheimer coefficient approach ($k_s^+ = 1/\alpha_y^+$) shows remarkably good agreement with the DNS data from Shahzad *et al.* [22], despite the subtle differences in design of the substrates. This suggests that the drag of perforated plates resembling acoustic liners indeed is dictated by the inverse of the viscous-scaled wall-normal Forchheimer permeability of the substrate, and that the permeable substrate we studied behaves as an acoustic liner due to the geometrical similarity.

C. Critical physical review of the theoretical framework

Given the results in this study, it can be considered challenging to experimentally realize a suitable combination of parameters for permeable substrates to achieve drag reduction in turbulent boundary layers. While the substrate in this study had the appropriate macroscopic permeability values for a predicted slip length and drag reduction, its physical realisation did not allow for significant slip at the surface interface, which is a difficulty that has repeatedly occurred in similar studies [25,28]. Moreover, in light of the theoretical framework, as we will show here, the substrate in this study did not meet the assumption on characteristic length scales, from hereon referred to as pore size assumption. This requirement for using the continuum approach is not further elaborated in the framework besides the statement that “pores are much smaller than any near-wall turbulent length scale” [7]. To facilitate the discussion, we assume the velocity profile penetration depth as the relevant flow length scale, since it defines the minimal wall-normal extent into the substrate wherein the continuum approach is applied to link the substrate permeability to the slip length via Brinkman’s equation. Furthermore, we assume that, in order to satisfy this condition such that the continuum approach can be applied, the substrate characteristic length scale or unit cell size should be at least an order of magnitude smaller than this velocity profile penetration depth, i.e., $\sqrt{K}/D > 10$, since $\sqrt{K} \approx \ell$ (see Sec. II A). For the present study, however, it is the expected penetration depth that is smaller than for example the pore depth ($\sqrt{K_x}/t \approx 0.3$) and unit cell size ($\sqrt{K_x}/d_y \approx 0.04$), where t is the wall thickness (and hence pore depth) and d_y indicates the unit cell size in wall-normal direction, as illustrated in Fig. 9.

To put the mismatch between substrate and flow length scales in this study into perspective, we discuss the general application of the theoretical framework to an experimental context. The framework does not take into account the physical relationship between permeable substrate length scales on the one hand, and the resulting macroscopic permeability on the other. This choice is understandable given that no analytical models exist that can predict the permeability of porous materials of arbitrary shapes. Even for simplified geometries, often semiempirical models are used. For an evaluation of different permeability models, the reader is referred to Refs. [42–44]. For the purpose of this discussion, we will consider the model from Carman [45] for the permeability of an isotropic porous medium of spherical objects, and the model from van der Westhuizen and Du Plessis [46] for the parallel permeability of a porous medium consisting of parallel circular rods (the envisioned implementation of streamwise-preferential permeable substrates in Ref. [7]). These models give a direct relationship between permeability, porosity, and a characteristic length scale, which in these cases are the diameter of the spheres and rods, respectively.

Table III shows instances of an isotropic bed of spheres configured in a hexagonal close-packed (HCP) lattice and an anisotropic structure of parallel rods in a hexagonal stacking lay-out for different porosity values. At $\epsilon = 0.5$, which is close to the value for the permeable substrate in this study, these structures would, based on their permeability, yield slip lengths and velocity profile penetration depths nearly two orders of magnitudes smaller than the substrate characteristic length scales or unit cell size. At $\epsilon = 0.8$, a value common in high-porosity foams and close to what was obtained through 3D printing by Efstathiou and Luhar [29], these ratios are still smaller than 1. Pushing the porosity to $\epsilon = 0.95$ would give ratios around one. This is still an order of magnitude lower than one would need to satisfy the pore size assumption from the theoretical framework. Note that the models were developed and validated with porosity values in the range of $\epsilon = 0.3$ – 0.5 , and that it is unknown to what extent predicted permeability values are valid at much higher porosity values. Nevertheless, we believe they provide a valid approximation and yield valuable insights within the scope of this discussion.

In conclusion, for realistic porosity values from a physical perspective, it is deemed unlikely that the pore size assumption from, and hence the continuum modeling approach taken in the theoretical framework, can be realized in a physical setting. Therefore it is questioned to what extent the macroscopic permeability values can be used as sole inputs for the purpose of predicting flow modulation effects and drag reduction values in turbulent boundary layers when applying the virtual origin framework to substrates with streamwise-preferential permeability. This work, alongside similar findings by Habibi Khorasani *et al.* [25], stresses the need for a good understanding of the relationship between macroscopic permeability of a permeable substrate, and its ability to facilitate slip at the flow-substrate interface given its (microscopic) physical structure there. We acknowledge that we have not validated these postulations with concrete facts obtained in this study and view them as potential open questions for future work. Last, considerable challenges in manufacturing such substrates, with streamwise-preferential permeability and very small characteristic length scales [$O(1\mu\text{m})$], are expected if one would pursue further experimental studies and ultimately industrially relevant applications.

V. CONCLUSIONS

Turbulent flows over substrates with streamwise-preferential permeability have been studied in the context of friction reduction. Direct force measurements and PIV experiments were conducted in the present study on a 3D-printed permeable structure. To our knowledge, the present work is the first experimental study in air flows in which the investigated substrate meets the requirements on the Darcy coefficient, or viscous permeability, for drag reduction based on the theoretical framework from Gómez-de Segura and García-Mayoral [7]. However, the observed drag increase of 0%–8% does not agree with the model predictions. We attribute this disparity to the absence of streamwise slip observed at the substrate-flow interface, which is a necessary condition for drag reduction in the virtual origin framework. Notably, the increase in drag matches DNS data from Shahzad

et al. [22] when using the inverse wall-normal Forchheimer coefficient, or inertial permeability, as the equivalent roughness parameter. The permeable structures in that study were designed as acoustic liners and are similar in geometrical properties to the one investigated in the present work. Consequently, this work constitutes the first experimental evidence that the wall-normal inertial permeability is the governing property for the drag behavior of acoustic liners, and further experimental studies to strengthen this hypothesis are encouraged.

The absence of slip is likely caused by the low pore area relative to the entire surface area of the substrate-flow interface, which implies that the majority of the surface imposes a strict no-slip condition on the flow. Moreover, the substrate characteristic length scales were larger than the expected velocity profile penetration depth based on the substrate permeability characteristics. These experimental setup limitations contrast with the length scale assumption foundational to the theoretical framework. However, with analytical models we derive that, for realistic, geometrically resolved cases, the characteristic length scales of permeable substrates are expected to be always larger than the slip length and penetration depth that they facilitate based on their corresponding permeability. Consequently, they cannot be modelled as a continuum for the virtual-origin approach. Therefore it is deemed unlikely that flow modulation behavior, and drag characteristics in particular, can be predicted for experimental settings using solely macroscopic permeability values. This is in line with recent findings from scale-resolved DNS by Habibi Khorasani *et al.* [25].

The theoretical framework from Gómez-de Segura and García-Mayoral [7] poses an elegant generalized approach to drag-reducing surface manipulations that puts substrates with streamwise-preferential permeability alongside proven methods such as superhydrophobic surfaces and riblets. However, the substrate idealisation as a continuum omits relevant characteristics of geometrically resolved porous structures. This stresses the need for a better understanding of the relationship between macroscopic permeability of a porous structure on the one hand, and how it interacts with the flow at the interface on the other. Based on the length-scale limitations and required physical properties, we expect that translating the abstraction of substrates with streamwise-preferential permeability into physical realisations relevant for practical drag reduction applications would result in structures very similar to riblets. Nevertheless, insights gained from future investigations into this topic could aid in the design of porous (meta-)materials for other applications where low-drag properties are relevant, such as acoustic liners, heat exchangers, and noise-reducing devices for turbulent boundary layer trailing-edge noise.

All data that support the findings of this study are included within the article.

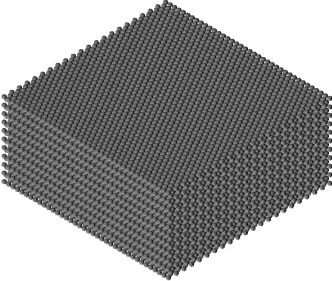
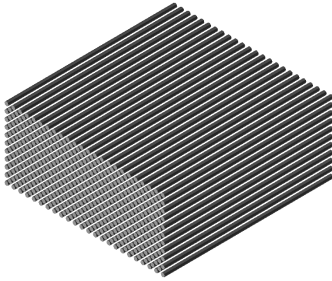
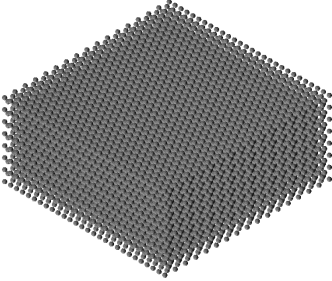
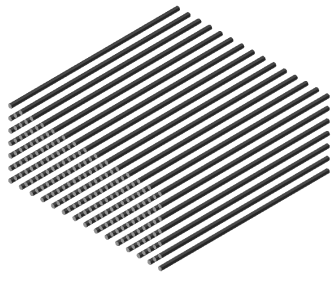
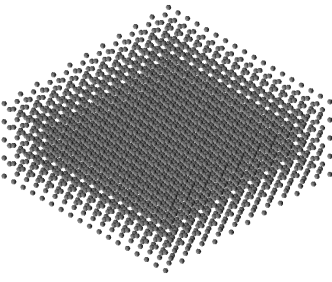
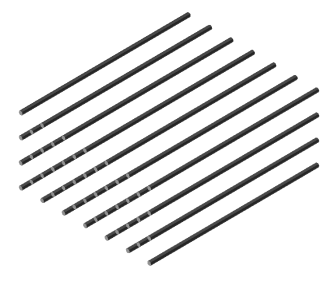
ACKNOWLEDGMENT

This work was in part financially supported by the Netherlands Enterprise Agency under Grant No. TSH21002. Experimental resources have been provided by Dimple Aerospace B.V.

APPENDIX

Table III shows examples of theoretical permeable substrates used for the discussion in Sec. IV C.

TABLE III. Instances of theoretical permeable substrates. HCP = hexagonal close packed.

	Isotropic bed of spheres in HCP lattice	Anisotropic structure of parallel rods
Length scale	Sphere diameter (D_p)	Rod/fibre diameter (D_f)
Unit cell size	$d_y = \sqrt[3]{\left(\frac{1}{1-\epsilon}\right) \frac{\pi D_p^3}{3\sqrt{2}}}$	$d_y = \sqrt{\left(\frac{1}{1-\epsilon}\right) \frac{\pi D_f^2}{2}}$
Permeability	$\frac{K}{D_p^2} = \frac{\epsilon^3}{180(1-\epsilon)^2}$ (Ref. [45])	$\frac{K_{\parallel}}{D_f^2} = \frac{(5.299 - 2.157\epsilon)\epsilon^2}{192(1-\epsilon)^2}$ (Ref. [46])
$\epsilon = 0.5$		
	$\sqrt{K}/D = 0.06, \sqrt{K}/d_y = 0.03$	$\sqrt{K}/D = 0.02, \sqrt{K}/d_y = 0.01$
$\epsilon = 0.8$		
	$\sqrt{K}/D = 0.3, \sqrt{K}/d_y = 0.1$	$\sqrt{K}/D = 0.3, \sqrt{K}/d_y = 0.1$
$\epsilon = 0.95$		
	$\sqrt{K}/D = 1.5, \sqrt{K}/d_y = 0.4$	$\sqrt{K}/D = 6.1, \sqrt{K}/d_y = 1.1$

- [1] M. J. Walsh, Riblets as a viscous drag reduction technique, *AIAA J.* **21**, 485 (1983).
- [2] H. Choi, P. Moin, and J. Kim, Direct numerical simulation of turbulent flow over riblets, *J. Fluid Mech.* **255**, 503 (1993).
- [3] R. García-Mayoral and J. Jiménez, Drag reduction by riblets, *Philos. Trans. R. Soc. A* **369**, 1412 (2011).
- [4] T. Min and J. Kim, Effects of hydrophobic surface on skin-friction drag, *Phys. Fluids* **16**, L55 (2004).
- [5] R. J. Daniello, N. E. Waterhouse, and J. P. Rothstein, Drag reduction in turbulent flows over superhydrophobic surfaces, *Phys. Fluids* **21**, 085103 (2009).
- [6] N. Abderrahaman-Elena and R. García-Mayoral, Analysis of anisotropically permeable surfaces for turbulent drag reduction, *Phys. Rev. Fluids* **2**, 114609 (2017).
- [7] G. Gómez-de-Segura and R. García-Mayoral, Turbulent drag reduction by anisotropic permeable substrates—Analysis and direct numerical simulations, *J. Fluid Mech.* **875**, 124 (2019).
- [8] F. Lovera and J. F. Kennedy, Friction-factors for flat-bed flows in sand channels, *J. Hydr. Div.* **95**, 1227 (1969).
- [9] J. F. Ruff and L. W. Gelhar, Turbulent shear flow in porous boundary, *J. Eng. Mech. Div.* **98**, 975 (1972).
- [10] R. T. Ho and L. W. Gelhar, Turbulent flow with wavy permeable boundaries, *J. Fluid Mech.* **58**, 403 (1973).
- [11] A. F. E. Zagni and K. V. H. Smith, Channel flow over permeable beds of graded spheres, *J. Hydr. Div.* **102**, 207 (1976).
- [12] F. Kong and J. Schetz, Turbulent boundary layer over porous surfaces with different surface geometries, in *20th Aerospace Sciences Meeting* (AIAA, Reston, VA, 1982).
- [13] H. J. Zippe and W. H. Graf, Turbulent boundary-layer flow over permeable and non-permeable rough surfaces, *J. Hydraul. Res.* **21**, 51 (1983).
- [14] Y. Shimizu, T. Tsujimoto, and H. Nakagawa, Experiment and macroscopic modelling of flow in highly permeable porous medium under free-surface flow, *J. Hydrosoci. Hydraul. Eng. Jpn.* **8**, 69 (1990).
- [15] D. Pokrajac and C. Manes, Velocity measurements of a free-surface turbulent flow penetrating a porous medium composed of uniform-size spheres, *Transp. Porous Media.* **78**, 367 (2009).
- [16] K. Suga, Y. Matsumura, Y. Ashitaka, S. Tominaga, and M. Kaneda, Effects of wall permeability on turbulence, *Int. J. Heat Fluid Flow* **31**, 974 (2010).
- [17] W. P. Breugem, B. J. Boersma, and R. E. Uittenbogaard, The influence of wall permeability on turbulent channel flow, *J. Fluid Mech.* **562**, 35 (2006).
- [18] Y. Kuwata and K. Suga, Lattice Boltzmann direct numerical simulation of interface turbulence over porous and rough walls, *Int. J. Heat Fluid Flow* **61**, 145 (2016).
- [19] K. Suga, Y. Nakagawa, and M. Kaneda, Spanwise turbulence structure over permeable walls, *J. Fluid Mech.* **822**, 186 (2017).
- [20] M. E. Rosti, L. Cortelezzi, and M. Quadrio, Direct numerical simulation of turbulent channel flow over porous walls, *J. Fluid Mech.* **784**, 396 (2015).
- [21] L. B. Esteban, E. Rodríguez-López, M. A. Ferreira, and B. Ganapathisubramani, Mean flow of turbulent boundary layers over porous substrates, *Phys. Rev. Fluids* **7**, 094603 (2022).
- [22] H. Shahzad, S. Hickel, and D. Modesti, Turbulence and added drag over acoustic liners, *J. Fluid Mech.* **965**, A10 (2023).
- [23] Q. Li, M. Pan, Q. Zhou, and Y. Dong, Turbulent drag modification in open channel flow over an anisotropic porous wall, *Phys. Fluids* **32**, 015117 (2020).
- [24] M. Itoh, S. Tamano, R. Iguchi, K. Yokota, N. Akino, R. Hino, and S. Kubo, Turbulent drag reduction by the seal fur surface, *Phys. Fluids* **18**, 065102 (2006).
- [25] S. M. Habibi Khorasani, M. Luhar, and S. Bagheri, Turbulent flows over porous lattices: alteration of near-wall turbulence and pore-flow amplitude modulation, *J. Fluid Mech.* **984**, A63 (2024).
- [26] M. E. Rosti, L. Brandt, and A. Pinelli, Turbulent channel flow over an anisotropic porous wall – drag increase and reduction, *J. Fluid Mech.* **842**, 381 (2018).
- [27] K. Suga, Y. Okazaki, U. Ho, and Y. Kuwata, Anisotropic wall permeability effects on turbulent channel flows, *J. Fluid Mech.* **855**, 983 (2018).
- [28] M. Morimoto, R. Aoki, Y. Kuwata, and K. Suga, Measurements for characteristics of turbulence over a streamwise preferential porous substrate, *Flow Turbul. Combust.* **113**, 71 (2024).

- [29] C. Efstathiou and M. Luhar, Turbulent boundary layers over streamwise-preferential porous materials, [arXiv:2006.00182](https://arxiv.org/abs/2006.00182).
- [30] F. H. Clauser, The turbulent boundary layer, in *Advances in Applied Mechanics* (Elsevier, Amsterdam, 1956), Vol. 4, pp. 1–51.
- [31] G. Gómez-de-Segura, A. Sharma, and R. García-Mayoral, Turbulent drag reduction using anisotropic permeable substrates, *Flow Turbul. Combust.* **100**, 995 (2018).
- [32] J. Nikuradse, *Laws of Flow in Rough Pipes* (National Advisory Committee for Aeronautics, Washington, DC, 1950).
- [33] M. D. M. Innocentini, A. R. F. Pardo, and V. C. Pandolfelli, Influence of air compressibility on the permeability evaluation of refractory castables, *J. Am. Ceram. Soc.* **83**, 1536 (2000).
- [34] A. Rubio Carpio, R. Merino Martínez, F. Avallone, D. Ragni, M. Snellen, and S. van der Zwaag, Experimental characterization of the turbulent boundary layer over a porous trailing edge for noise abatement, *J. Sound Vib.* **443**, 537 (2019).
- [35] C. Efstathiou and M. Luhar, Mean turbulence statistics in boundary layers over high-porosity foams, *J. Fluid Mech.* **841**, 351 (2018).
- [36] M. van Nesselrooij, O. W. G. Van Campenhout, B. W. Van Oudheusden, F. F. J. Schrijer, and L. L. M. Veldhuis, Development of an experimental apparatus for flat plate drag measurements and considerations for such measurements, *Meas. Sci. Technol.* **33**, 055303 (2022).
- [37] O. W. G. van Campenhout, M. van Nesselrooij, Y. Y. Lin, J. Casacuberta, B. W. van Oudheusden, and S. Hickel, Experimental and numerical investigation into the drag performance of dimpled surfaces in a turbulent boundary layer, *Int. J. Heat Fluid Flow* **100**, 109110 (2023).
- [38] A. Sciacchitano and B. Wieneke, PIV uncertainty propagation, *Meas. Sci. Technol.* **27**, 084006 (2016).
- [39] E. Rodríguez-López, P. J. K. Bruce, and O. R. H. Buxton, A robust post-processing method to determine skin friction in turbulent boundary layers from the velocity profile, *Exp. Fluids* **56**, 68 (2015).
- [40] P. Schlatter and R. Örlü, Assessment of direct numerical simulation data of turbulent boundary layers, *J. Fluid Mech.* **659**, 116 (2010).
- [41] A. Chavarin, C. Efstathiou, S. Vijay, and M. Luhar, Resolvent-based design and experimental testing of porous materials for passive turbulence control, *Int. J. Heat Fluid Flow* **86**, 108722 (2020).
- [42] M. A. F. Zarandi, S. Arroyo, and K. M. Pillai, Longitudinal and transverse flows in fiber tows: Evaluation of theoretical permeability models through numerical predictions and experimental measurements, *Compos. Part A: Appl. Sci. Manuf.* **119**, 73 (2019).
- [43] G. W. Jackson and D. F. James, The permeability of fibrous porous media, *Can. J. Chem. Eng.* **64**, 364 (1986).
- [44] B. T. Åström, R. B. Pipes, and S. G. Advani, On flow through aligned fiber beds and its application to composites processing, *J. Compos. Mater.* **26**, 1351 (1992).
- [45] P. C. Carman, *Flow of Gases through Porous Media* (Academic Press, New York, 1956).
- [46] J. Van der Westhuis and J. P. Du Plessis, An attempt to quantify fibre bed permeability utilizing the phase average Navier–Stokes equation, *Compos. Part A: Appl. Sci. Manuf.* **27**, 263 (1996).